Supplemental Information for "Quantum erasure using surface acoustic phonons"

DEVICE, EXPERIMENTAL SETUP AND TECHNIQUES

The flip-chip device, setup and techniques used for this experiment are strictly identical to [1], except that the data shown in this paper were acquired in a separate cool-down of the cryostat used for the experiment (base temperature < 7 mK). A full wiring diagram and a description of the room-temperature set-up may be found in Ref. [2]. The fabrication description is given in Ref. [3]. The circuit is shown in Fig. S1. Compared to Ref. [1], we note a 5% shift in the nominal values of the Josephson junctions of the two tunable couplers, as well as an overall reduction of the coherence times of the qubits.

For this run, we implemented in addition a three-state dispersive readout. Each qubit readout resonator is a $\lambda/4$ resonator inductively coupled to a $\lambda/2$ Purcell filter. A 500-ns microwave tone is applied at resonance with each qubit readout resonator and the transmitted signal is successively amplified by a traveling-wave parametric amplifier [4], a high-electron mobility transistor amplifier, and a room-temperature amplifier, before homodyne mixing and recording the integrated value of the quadrature amplitudes I and Q. To estimate the fidelity of the preparation and readout of each state, we successively prepare each qubit in $|g\rangle$, $|e\rangle$ or $|f\rangle$ and repeat each measurement 4000 times. The state-dependent dispersive shift of the readout resonator allows us to attribute a sector of the IQ plane to each state, enabling us to identify the qubit state from any single-shot readout based on its recorded I and Q values. These calibrations also determine the fidelity of each state readout, which are all above 90%, see Table S1. Data shown in Fig. 3 and Fig. 4b in the main text are corrected for readout errors using this calibration.

To perform a delayed-choice quantum eraser test, we modified the Q_1 measurement procedure to fit within a phonon round-trip time, by shortening its readout pulse from 500 ns to 200 ns. When performing a two-state

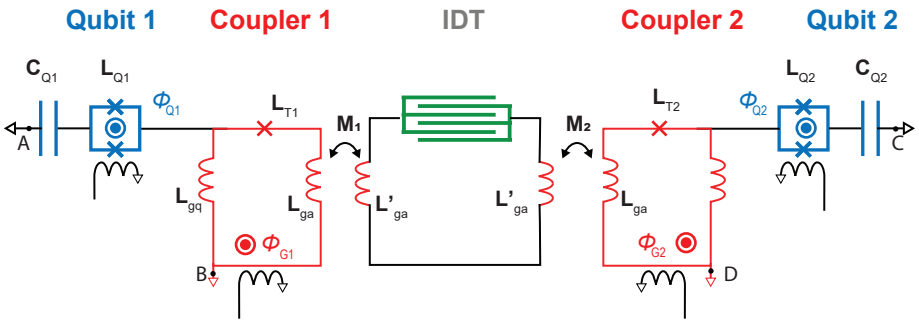

Figure S1. Electrical circuit. Elements in blue are the qubit equivalent circuits, in red the variable couplers and the inductive couplers between the qubit sapphire chip and the acoustic lithium niobate chip, and green the interdigitated transducer (IDT) for phonon emission and capture.

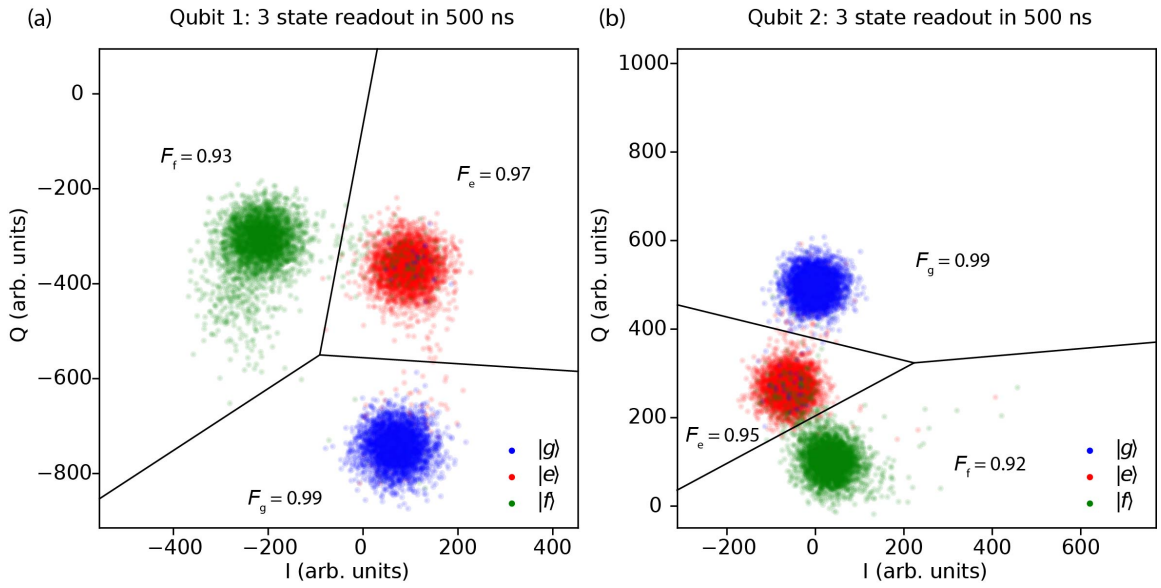

Figure S2. Qubits Q_1 (a) and Q_2 (b) single-shot readout using a 500-ns readout pulse. Dots indicate the coordinates in the IQ-plane of each integrated integrated readout pulses for the 4000 measurements realized after preparing each qubit either in $|g\rangle$ (blue), $|e\rangle$ (red) or $|f\rangle$ (green). This calibration allows us to assign any given measurement to the ground, excited or second excited state, as separated by the black lines in the IQ plane. Corresponding fidelities are given in inset.

readout, this decreases the visibility of Q_1's $|e\rangle$ and $|g\rangle$ states to 81%.

RELAXATION RATES AND CIRCUIT MODELING

In this section, we describe the modeling and the measurements of the relaxation rates when one qubit (Q_1) is maximally coupled to the IDT, and the other qubit is disconnected (coupler 2 turned off), see Fig. 2 in the main text. For a given qubit frequency, the operating points are determined by (1) maximizing the coupler-induced frequency shift on the qubit, (2) maximizing the other qubit relaxation time. We prepare the qubit in $|e\rangle$ or $|f\rangle$ by the successive application of resonant π pulses and measure the qubit state populations after a varying amount of time t during which coupler 1 is open. The measurements realized on Q_1 for the two operating points described in the main text are shown in Fig. S3.

A weakly anharmonic transmon- or xmon-style qubit is expected to have decay rates very similar to a harmonic oscillator [5], with the population of the $|e\rangle$ and $|f\rangle$ excited states evolving as

$$\dot{P}_f = -\kappa_{ef} P_f - \kappa_{gf} P_f \tag{S1}$$

$$\dot{P}_e = -\kappa_{ge} P_e + \kappa_{ef} P_f, \tag{S2}$$

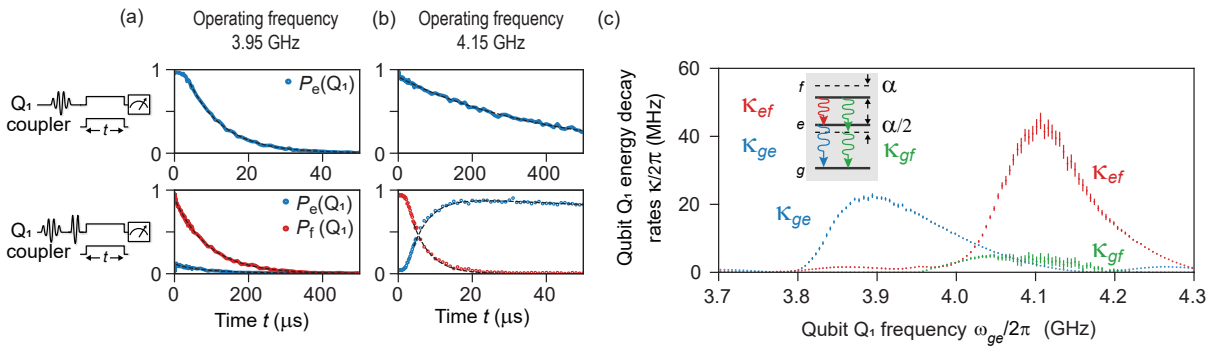

Figure S3. (a-b) Q_1 energy decay rates are extracted for its first two transitions, κ_{ge} and κ_{ef} at two operating points, $\omega_{ge}/2\pi = 3.95$ GHz (panel a) and $\omega_{ge}/2\pi = 4.15$ GHz (panel b). The decay rates are fit from the exponential decay of Q_1's state populations after excitation to $|e\rangle$ ($|f\rangle$), see top (bottom) panels. Dashed lines are the fits described in the text. (c) Extracted Q_1 energy decay rates when including a direct two-phonon relaxation from $|f\rangle$ to $|g\rangle$ with rate κ_{gf}.

where $\kappa_{ef} = 2\kappa_{ge}$ and $\kappa_{gf} = 0$. Here, due to the IDT response, we measure a very different behavior.

We first make the assumption that $\kappa_{gf} = 0$, as this two-phonon relaxation is expected to be exponentially suppressed for a transmon [5]. To determine the rates κ_{ge} and κ_{ef}, we start by fitting the decay from $|e\rangle$ after excitation to $|e\rangle$ with a single decaying exponential for all qubit frequencies. We only consider times past the transient on-set of the coupler ($t \geq 3$ ns) and prior to any re-excitation of the qubit by the phonons reflected off the mirrors ($t < 500$ ns) when within the mirrors' bandwidth. We also fix the steady-state populations by measuring the qubit population without any microwave excitation. This fit determines κ_{ge}.

We repeat the same single decaying exponential fit for the decay from $|f\rangle$ after excitation to $|f\rangle$, determining κ_{ef}. The $|e\rangle$ population evolution after excitation to $|f\rangle$ is modeled by Eq. S2 using the two fitted rates. The resulting fits are shown in Fig. S3 for the operating frequencies ω_A and ω_B defined in the main text for Q_1, and agree very well with the data. The frequency dependence of κ_{ge} and κ_{ef} is shown in Fig. 2 of the main text.

We now consider the possibility of a two-phonon relaxation process, under the hypothesis that it could be strongly enhanced due to the frequency dependence of the IDT [6]. The two-phonon relaxation is expected to be maximal when $\omega_{ge} - |\alpha|/2$ matches the IDT central frequency. We fit the population evolution from $|f\rangle$ using a two-parameter fit and keeping κ_{ge} as given by fitting the decay from $|e\rangle$ after excitation to $|e\rangle$. The result is shown in Fig. S3c. The extracted κ_{gf} reaches a maximum of $1/30$ ns. At the operating frequencies of the main text, ω_A and ω_B, the ratio κ_{gf}/κ_{ef} is below 10%. The uncertainty of this determination is also quite large when κ_{ef} is large - more than 50% whenever $\kappa_{ef}/2\pi \leqslant 20$ MHz. We thus conclude that even if this process occurs, it is negligible in our experiment.

We attempted to model the frequency-dependent relaxation rates using a circuit model for the qubit-coupler-IDT system. The IDT is modeled using a coupling-of-modes model [7], taking into account the internal reflections oc-

curring between the electrodes of the IDT, thus allowing us to infer the IDT admittance as a function of frequency, see Fig. S4a. For reference, we also study the ideal case of an uniform transducer with no internal reflections, where the IDT admittance is given by

$$Y_a(\omega) = iC_0\omega + G_a(\omega) + iB_a(\omega), \tag{S3}$$

where C_0 is the IDT electrical capacitance, $G_a(\omega)$ the IDT conductance given in the main text, and B_a the IDT susceptance related to its conductance by an Hilbert transformation $B_a(\omega) = G_a(\omega) * [-1/\pi\omega]$. We then derive the equivalent impedance $Z(\omega)$ for the circuit shown in Fig. S1 looking into terminals A-B for qubit Q_1 (or C-D for qubit Q_2). We extract the circuit resonant frequencies by looking for the zeros of $Z(\omega)$ in the complex plane. Ignoring losses in the IDT (by setting $\mathrm{Re}[Y(\omega)] = 0$), we identify three modes: the qubit, the IDT series resonance, and the mode created by the IDT capacitor and the couplers' inductance networks. We then re-evaluate the frequencies of these modes in the presence of IDT loss. To extract the qubit relaxation rate and its anharmonicity, we approximate the circuit near the qubit resonance ω_q as an RLC series circuit, with effective parameters

$$L_{\mathrm{eff}} = 2/\mathrm{Im}[Z'(\omega_q)], \tag{S4}$$

$$C_{\mathrm{eff}} = 1/(L_{\mathrm{eff}}\omega_q^2), \tag{S5}$$

$$R_{\mathrm{eff}} = \mathrm{Re}[Z(\omega_q)]. \tag{S6}$$

The qubit relaxation rate $\kappa_{ge} = 1/T_1$ is then given by $T_1\omega_q = Q$, where the qubit quality factor is given by $Q = \frac{\sqrt{L_{\mathrm{eff}}/C_{\mathrm{eff}}}}{R_{\mathrm{eff}}}$. To evaluate the anharmonicity, we split the effective qubit inductance L_{eff} into its non-linear part, arising from the qubit SQUID inductance $L_q(\phi_q)$, and its linear part $L_{\mathrm{eff}} - L_q(\phi_q)$. The anharmonicity is then given by [8]:

$$\alpha = -\frac{e^2}{2C_{\mathrm{eff}}}\left(\frac{L_q(\phi_q)}{L_{\mathrm{eff}}}\right)^3. \tag{S7}$$

Finally, the relaxation rate from state $|f\rangle$ is given by $\kappa_{ef} = 2/T_{1,ef}$ where $T_{1,\mathrm{ef}} \times (\omega_q + \alpha) = Q_{\mathrm{ef}}$ and Q_{ef} is evaluated considering the following updated circuit parameters:

$$L_{\mathrm{eff,ef}} = 2/\mathrm{Im}[Z'(\omega_q + \alpha)], \tag{S8}$$

$$C_{\mathrm{eff,ef}} = 1/[L_{\mathrm{eff,ef}}(\omega_q + \alpha)^2], \tag{S9}$$

$$R_{\mathrm{eff,ef}} = \mathrm{Re}[Z(\omega_q + \alpha)], \tag{S10}$$

$$Q_{\mathrm{ef}} = \frac{\sqrt{L_{\mathrm{eff,ef}}/C_{\mathrm{eff,ef}}}}{R_{\mathrm{eff,ef}}}. \tag{S11}$$

To obtain the model relaxation rates shown in Fig. 2 of the main text, we use the parameters listed in Table S1 as input parameters. The non-design parameters were calibrated as follow: The qubit capacitance was adjusted to reproduce the qubit anharmonicity and the qubit SQUID inductance was adjusted to reproduce the measured qubit

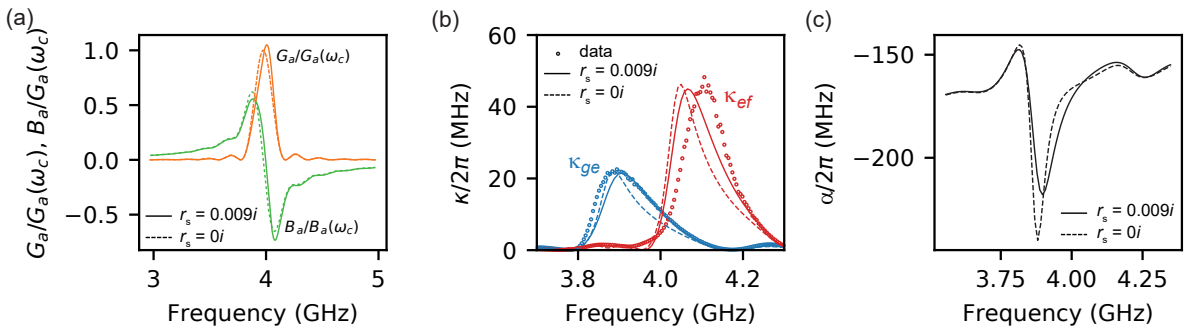

Figure S4. (a) Conductance (orange) and susceptance (green) for a 20 finger pairs uniform IDT, with no internal reflectivity (dashed lines) and a small reflectivity (solid lines). (b) Energy decay rates κ_{ge} (blue) and κ_{ef} (red) extracted for the electrical circuit considered in Fig. S1, as detailed in the text, considering a non-reflective transducer (dashed lines, $r = 0$, $M = 0.23$ pH) and a small amount of internal reflections (solid lines, $r = 0.009j$, $M = 0.21$ pH). The mutual coupling between the two chips was adjusted to reproduce the height of the κ_{ge} peak. (c) Induced qubit anharmonicity for both types of transducers. The error in κ_{ef} seems to arise from an overestimate of the anharmonicity.

bare frequency. The couplers' Josephson junction inductances were calibrated using the qubit frequency shift induced by the coupler, with the qubit tuned at a non-zero emission point for the IDT. The mutual inductive coupling between the two chips was calibrated using the qubit-qubit direct electrical coupling ($\sim g/2\pi = 1.1$ MHz) at a non-zero emission point for the IDT. The SAW velocity for the IDT was adjusted to match the frequencies of the two zero emission points. Finally the IDT reflectivity r is an imaginary free parameter, whose value is expected to be small ($|r| \lesssim 1\%$) for a 30-nm-thick aluminum transducer fabricated on a $128°Y - X$ lithium niobate wafer [7].

The IDT internal reflectivity ($r = 0.009i$) and the mutual inductance ($M = 0.23$ pH) between the chips are adjusted to match as closely as possible the κ_{eg} curve. As can be seen in Fig. 2 of the main text, this model can reproduce qualitatively the κ_{eg} rates, but only roughly matches the κ_{ef} measured rates, with a significant 50-MHz discrepancy for the κ_{ef} maximum. Tuning the parameters of the IDT (capacitance and reflectivity) and of the coupling circuit (mutual inductance between the flip-chips and the couplers' junction inductances) does not give a better agreement.

By comparing the model derived using the simple symmetric IDT admittance given by Eq. S3, see Fig. S4, we see that most of the asymmetry of the κ_{eg} curve is actually due to the coupling of the qubit to the IDT, and not to the internal reflections of the IDT. This can be understood as the Lamb shift induced on the qubit [6] when coupled to the IDT, which is related to $B_a(\omega)$ [6] and which also induces a frequency dependence for the qubit anharmonicity when coupled to the IDT.

NUMERICAL MODELING

In this last section, we address the numerical modeling of the quantum eraser experiment, as well as the transfers from Fig. 3 in the main text. In the quantum eraser experiment, the system comprises two qubits (Q_1 and Q_2 and the itinerant wavepackets corresponding to the phonons A and B.

We model the qubits as anharmonic oscillators with bosonic creation operators $\hat{s}_i$. Their non-interacting Hamiltonians in the frame rotating at the frequency of phonon A is given by

$$H_{0,i}/\hbar = \Delta_i \hat{s}_i^\dagger \hat{s}_i + \alpha_i \hat{s}_i^\dagger \hat{s}_i^\dagger \hat{s}_i \hat{s}_i, \tag{S12}$$

where Δ_i is the detuning of qubit i with respect to phonon A and α_i its anharmonicity. We also define the qubit matrix element operators $\hat{s}_{\mathrm{ge},i} = |g\rangle\langle e|$ and $\hat{s}_{\mathrm{ef},i} = |e\rangle\langle f|$ to take into account transition-dependent effects.

The itinerant wavepackets are modeled as bosonic modes. To accurately describe the emission and capture of the phonons, and model the evolution of the populations in these itinerant bosonic modes, we use the theory derived in [9]. Each interaction of the qubits with the acoustic channel requires the use of two wavepackets: an input wavepacket and an output wavepacket. As we wish to model four interactions (the half-emission (or the herald emission) and the half-phonon capture (or the herald capture) for phonon mode A (or B)), we only need to consider six wavepackets: First, $a_{\mathrm{in}}(t)$ ($b_{\mathrm{in}}(t)$), the input acoustic field that interacts with qubit Q_1 during the phonon A (B) emission at time $t_{e,A}$ ($t_{e,B}$). Second, $a_{\mathrm{rt}}(t)$ ($b_{\mathrm{rt}}(t)$) is the acoustic output field describing the result from the interaction of $a_{\mathrm{in}}(t)$ ($b_{\mathrm{in}}(t)$) with the qubit and contains the emitted phonon A (B). This field will then be used as input for the second interaction with the qubit after it completes one round-trip during the capture process. Third, the field $c_{\mathrm{out}}(t)$ ($b_{\mathrm{out}}(t)$), the acoustic output field containing the phonon resulting from this second interaction. According to [9], bosonic annihilation operators can be used to describe the quantum state contained in these wavepackets, defined as

$$\hat{w} = \int w(t) u_w(t) dt, \tag{S13}$$

where the functions $u_w(t)$ describe the wavepacket envelopes and are normalized such that $\int |u_w(t)|^2 dt = 1$.

To describe the interactions of the qubits with the acoustic channel during the quantum eraser experiment, we thus use six bosonic creation operators, three ($\hat{a}_{\mathrm{in}}$, $\hat{a}_{\mathrm{rt}}$, and $\hat{a}_{\mathrm{out}}$) for the half-phonon and three ($\hat{b}_{\mathrm{in}}$, $\hat{b}_{\mathrm{rt}}$, and $\hat{b}_{\mathrm{out}}$) for the heralding phonon. We note that $\hat{a}_{\mathrm{rt}}$ and $\hat{b}_{\mathrm{rt}}$ correspond to what we call phonons A and B in the main text.

In the frame rotating at the phonon A emission frequency, the stationary Hamiltonian of the system is

$$H_0/\hbar = \sum_{i=1,2} H_{0,i}/\hbar + \sum_{i=\mathrm{in,rt,out}} \Delta_{b,i} \hat{b}_i^\dagger \hat{b}_i \tag{S14}$$

where $\Delta_{b,i}$ is the detuning of phonon B with respect to the frequency of phonon A.

The interaction of the sub-system comprising one incoming bosonic mode $\hat{a}_x$ and one outgoing bosonic mode $\hat{a}_y$ interacting with one of the qubits at time t, either on its g-e or e-f transition, $\hat{c} = \hat{s}_{\mathrm{ge},i}$ or $\hat{c} = \hat{s}_{\mathrm{ef},i}$, at the coupling rate $\kappa_i(t)$ set by the coupler, is described by this master equation:

$$\dot{\rho}(t) = -\frac{i}{\hbar}[\rho(t), \hat{H}(t)] + \hat{L}_0 \rho \hat{L}_0^\dagger - \frac{1}{2}\{\hat{L}_0^\dagger \hat{L}_0, \rho(t)\}, \tag{S15}$$

where the Hamiltonian $\hat{H}(t)$ is given by

$$\hat{H}/\hbar = \hat{H}_0/\hbar + \frac{i}{2}\left(\sqrt{\kappa_i(t)} g_{\mathrm{in}}^*(t) \hat{a}_x^\dagger \hat{c} + \sqrt{\kappa_i(t)} g_{\mathrm{out}}(t) \hat{c}^\dagger \hat{a}_y + g_{\mathrm{in}}^*(t) g_{\mathrm{out}}(t) \hat{a}_x^\dagger \hat{a}_y - h.c.\right), \tag{S16}$$

and the Lindblad operator is given by

$$\hat{L}_0(t) = \sqrt{\kappa_i(t)}\hat{c} + g_{\mathrm{in}}(t)\hat{a}_x + g_{\mathrm{out}}(t)\hat{a}_y. \tag{S17}$$

In the above equations, the coupling coefficients are given by

$$g_{\mathrm{in}}(t') = \frac{\sqrt{\kappa_c}}{\sqrt{1 + e^{-\kappa_c t'}}}, \text{ and} \tag{S18}$$

$$g_{\mathrm{out}}(t') = -\frac{\sqrt{\kappa_c}}{\sqrt{1 + e^{\kappa_c t'}}}, \tag{S19}$$

using the cosecant wavepackets from the experiment.

We simulate the total evolution of the system using four consecutive integrations of Eq. S15. In addition, we include the action of qubit decoherence and acoustic losses by including the following Lindblad dissipation operators: $\sqrt{1/T_1}\hat{s}_i$ for the intrinsic qubit relaxation, $\sqrt{1/T_\phi}\hat{s}_{\mathrm{ge}}^\dagger \hat{s}_{\mathrm{ge}}$ and $\sqrt{1/T_\phi}\hat{s}_{\mathrm{ef}}^\dagger \hat{s}_{\mathrm{ef}}$ for the qubit decoherence for the g-e and e-f transitions, with $1/T_{\phi,\mathrm{ge|ef}} = 1/T_{2,R,\mathrm{ge|ef}} - 1/(2T_1)$, and $\sqrt{\kappa_a}\hat{a}$, $\sqrt{\kappa_b}\hat{b}$ for the acoustic losses, with κ_a and κ_b defined to match the round-trip transfer efficiency $\eta_a = e^{-\kappa_a \tau}$ and $\eta_b = e^{-\kappa_b \tau}$. The qubits' XY drives are modeled using $H_D/\hbar = \beta(\hat{s}_i e^{i\omega_d t} + \hat{s}_i^\dagger e^{-i\omega_d t})$, where β is adjusted to give the measured rotation.

We perform these master equations simulations using QuTip [10], with the control sequences defined in Fig. 3 and 4 of the main text as inputs. The model input parameters are given in Table S1. The extracted populations are shown in Fig. 3 and 4 of the main text, corrected for readout errors only in Fig. 4b, and giving good agreement with the measured data.

Qubit parameters	Qubit 1	Qubit 2
Qubit bare frequency (GHz)	4.86	~ 6
Qubit capacitance (fF)	100	100
SQUID inductance (nH)	10.4	7.0
Qubit anharmonicity (MHz)	-179	-188
Qubit intrinsic lifetime, eg transition, $T_{1,eg,\mathrm{int}}$ (μs)	18	18
Qubit intrinsic lifetime, ef transition, $T_{1,ef,\mathrm{int}}$ (μs)	11	11
Qubit Ramsey dephasing time, eg transition, $T_{2,ge,\mathrm{Ramsey}}$ (μs)	1.2	0.8
Qubit Ramsey dephasing time, ef transition, $T_{2,ef,\mathrm{Ramsey}}$ (μs)	0.4	0.4
$\|f\rangle$ state readout fidelity	0.93	0.92
$\|e\rangle$ state readout fidelity	0.97	0.95
$\|g\rangle$ state readout fidelity	0.99	0.99

Tunable coupler parameters	Coupler 1	Coupler 2
Coupler junction inductance (nH)	1.19	1.24
IDT grounding inductance (design value) (nH)	0.4	0.4
Coupler grounding inductance (design value) (nH)	0.4	0.4
Mutual coupling inductance between IDT and coupler (nH)	0.21	0.21

SAW resonator parameters	Free space	Mirror	Transducer
Aperture (μm)		75	75
Wave propagation speed (km/s)	4.034(2)	3.928(2)	3.911(2)
Wave propagation losses (Np/m)	70(10)	-	-
Number of cells		400	20
Pitch (μm)		0.5	0.985
Reflectivity		-0.049i(5)	0.009i(2)
Metallization ratio		0.58	0.58
Effective mirror-mirror distance (μm)		2029.6	
Free spectral range (MHz)		1.97	

Table S1. Device parameters for the two qubits, parameters related to the interdigitated acoustic transducer (IDT), the tunable couplers connecting each qubit to the SAW resonator, and the SAW resonator itself.

[1] A. Bienfait, K. J. Satzinger, Y. P. Zhong, H.-S. Chang, M.-H. Chou, C. R. Conner, É Dumur, J. Grebel, G. A. Peairs, R. G. Povey, and A. N. Cleland, "Phonon-mediated quantum state transfer and remote qubit entanglement," Science **364**, 368–371 (2019).

[2] Y. P. Zhong, H.-S. Chang, K. J. Satzinger, M.-H. Chou, A. Bienfait, C. R. Conner, É. Dumur, J. Grebel, G. A. Peairs, R. G. Povey, D. I. Schuster, and A. N. Cleland, "Violating Bell's inequality with remotely connected superconducting qubits," Nature Physics **15**, 741–744 (2019).

[3] K. J. Satzinger, Y. P. Zhong, H.-S. Chang, G. A. Peairs, A. Bienfait, Ming-Han Chou, A. Y. Cleland, C. R. Conner, É. Dumur, J. Grebel, I. Gutierrez, B. H. November, R. G. Povey, S. J. Whiteley, D. D. Awschalom, D. I. Schuster, and A. N. Cleland, "Quantum Control of Surface Acoustic-Wave Phonons," Nature **563**, 661–665 (2018).

[4] C. Macklin, K. O'Brien, D. Hover, M. E. Schwartz, V. Bolkhovsky, X. Zhang, W. D. Oliver, and I. Siddiqi, "A near–quantum-limited Josephson traveling-wave parametric amplifier," Science **350**, 307–310 (2015).

[5] J. Koch, T. M. Yu, J. Gambetta, A. A. Houck, D. I. Schuster, J. Majer, A. Blais, M. H. Devoret, S. M. Girvin, and R. J. Schoelkopf, "Charge-insensitive qubit design derived from the Cooper pair box," Phys. Rev. A **76**, 042319 (2007).

[6] Anton Frisk Kockum, Per Delsing, and Göran Johansson, "Designing frequency-dependent relaxation rates and Lamb shifts for a giant artificial atom," Physical Review A **90**, 013837 (2014).

[7] David Morgan, *Surface Acoustic Wave Filters* (Elsevier, 2007).

[8] Yu Chen, C. Neill, P. Roushan, N. Leung, M. Fang, R. Barends, J. Kelly, B. Campbell, Z. Chen, B. Chiaro, A. Dunsworth, E. Jeffrey, A. Megrant, J. Y. Mutus, P. J. J. O'Malley, C. M. Quintana, D. Sank, A. Vainsencher, J. Wenner, T. C. White, Michael R. Geller, A. N. Cleland, and John M. Martinis, "Qubit Architecture with High Coherence and Fast Tunable Coupling," Physical Review Letters **113**, 220502 (2014).

[9] Alexander Holm Kiilerich and Klaus Mølmer, "Input-Output Theory with Quantum Pulses," Physical Review Letters **123**, 123604 (2019).

[10] J. R. Johansson, P. D. Nation, and Franco Nori, "QuTiP: An open-source Python framework for the dynamics of open quantum systems," Computer Physics Communications **183**, 1760–1772 (2012).